Exp Brain Res (2001) 136:492–506
DOI 10.1007/s002210000598

RESEARCH ARTICLE

Christopher D. Mah

Spatial and temporal modulation of joint stiffness during multijoint movement

Received: 29 October 1999 / Accepted: 22 September 2000 / Published online: 6 December 2000

Abstract Joint stiffness measurements during small transient perturbations have suggested that stiffness during movement is different from that observed during posture. These observations are problematic for theories like the classical equilibrium point hypothesis, which suggest that desired trajectories during movement are enforced by joint stiffness. We measured arm impedances during large, slow perturbations to obtain detailed information about the spatial and temporal modulation of stiffness and viscosity during movement. While our measurements of stiffness magnitudes during movement generally agreed with the results of measurements using fast perturbations, they revealed that joint stiffness undergoes stereotyped changes in magnitude and aspect ratio which depend on the direction of movement and show a strong dependence on joint angles. Movement simulations using measured parameters show that the measured modulation of impedance acts as an energy conserving force field to constrain movement. This mechanism allows for a computationally simplified account of the execution of multijoint movement. While our measurements do not rule out a role for afferent feedback in force generation, the observed stereotyped restoring forces can allow a dramatic relaxation of the accuracy requirements for forces generated by other control mechanisms, such as inverse dynamical models.

Keywords Human · Multijoint movement · Stiffness · Impedance · Arm

Introduction

Observations of joint stiffness during motion suggest that the effective mechanical response of the arm during voluntary movement is different from that seen at rest (Bennet et al. 1992; Bennet 1994; Gomi and Kawato 1996). While the mass and shape of the arm do not change significantly during movement, elastic and viscous forces which depend on the physiological state of muscles are altered during movement and when muscles are active (Milner 1993). The modulation of effective mechanical properties during movement offers the possibility that the control of movement execution by the CNS might be simplified by a suitable choice of the sequence of mechanical states of the arm, prior to movement onset (Lacquaniti et al. 1992; Towhidkhah et al. 1997). Specifically, different levels of stiffness might be appropriate at different times to correct errors while avoiding unnecessary muscle activity.

Without elastic restoring forces, a small error in computed or produced torques early in a multijoint movement can lead to large position errors at the end of the movement. The classical equilibrium point hypothesis (in several forms) avoids this difficulty by postulating that neural commands specify end and intermediate points on the movement, and that the details of force feedback are determined by mechanical and reflex properties of muscle (Feldman 1966; Bizzi et al. 1984; Flash 1987). However, observations of stiffness magnitudes during movement are incompatible with simpler forms of this hypothesis (Gomi and Kawato 1996; Gomi and Kawato 1997). In this paper we present data and simulations which suggest that modulation of arm impedance during movement can account both for existing observations on stiffness during movement, and for the robust control of voluntary movement.

Joint stiffness measurements during motion have predominantly involved small (Bennet et al. 1992; Bennet 1994) and/or transient (Gomi and Kawato 1996) perturbations in order to preclude voluntary intervention by the subject. The same approach has been taken in several investigations of postural stiffness, for example in the work of Tsuji et al. (1995) and Gomi and Osu (1998). However, it is possible that such perturbations induce reflex mechanisms which are not normally active during voluntary movement (Bennet 1994) or produce anomalous

C.D. Mah (✉)
Department of Physical Medicine and Rehabilitation,
Northwestern University, 345 East Superior St.,
Chicago, IL 60611, USA
e-mail: c-mah@northwestern.edu
Fax: +1-312-2382208

results because of inappropriate models for force-velocity relationships in normal muscle (Gribble et al. 1998; Karniel and Inbar 1997). In addition, this choice of perturbations has limited the data available on the detailed spatial and temporal pattern of stiffness and viscosity during multijoint movements. A number of prior studies have suggested that the human subject can suppress a voluntary response for more than 700 ms (e.g., Bennet et al. 1992; Gomi et al. 1992; Shadmehr et al. 1993; Latash 1994). Therefore, we attempted to extend the observations of Won and Hogan (1995) and the conclusions of Gribble et al. (1998) using a systematic but unpredictable set of perturbations to slowly alter multijoint movement over its entire course.

The influence of constraint forces on the behavior of mechanical systems can be dramatic, as for example when a playground slide produces inclined rather than vertical motion of a falling body, and this constraint continues to shape movement even when forces other than gravity are applied. Thus, motion can be dramatically affected by passive forces in the absence of an equilibrium point. The principle of constraint is to prevent motion in the constraint direction while storing as little elastic energy as possible. Our simulations compared the efficacy of joint stiffness modulation in controlling the limb trajectory through energy-conserving, and non-energy-conserving mechanisms. This comparison tested the hypothesis that postural stiffness mechanisms implement trajectory stability during multijoint movement through a constraint mechanism.

Since voluntary movement is variable, the nominal trajectory for any perturbed movement is not known. In order to estimate the relationship between trajectory error and restoring force on a trial by trial basis it is necessary to use perturbations which are larger than the movement variability. This size requirement is analogous to the fact that due to local inhomogeneities in topography, a sufficiently long journey is necessary to accurately estimate the curvature of the earth. Our data suggest that stiffness is modified during movement, depending on the movement context as well as the geometrical and physical properties of the limb. Movement context is taken to mean the direction of intended movement, and the stage of movement during which the perturbation and measurement takes place. A non-linear model of passive stiffness and viscosity is required to account for restoring forces in response to moderate and large perturbations, though these responses appear to remain energetically passive. Finally, our simulations suggest that the role of joint stiffness during unperturbed movement can be adequately described by a linearized time-varying model of stiffness (Slotine and Li 1991).

Materials and methods

Experimental methods

Five male subjects participated in the experiment after giving informed consent according to the standards of the Institutional Review Board of Northwestern University. With their right hands, subjects held the handle of a two-joint robot manipulandum which controlled the position of a cursor on a screen placed just above eye level (Fig. 1A). The manipulandum was free to move in the horizontal plane. Chair position was adjusted so that the hand was placed at the center of the workspace in the intersection of sagittal and horizontal planes at an elbow angle of 90 degrees, and the wrist was immobilized by a cast. A 6-*df* force sensor (ATI technologies F/T Gamma 30/100) mounted in the handle measured the interaction force between the subject's hand and the manipulandum. The trial began when the subject moved the cursor to a fixed starting point. When the cursor attained the starting point, there was a 1-s tone. At tone offset, subjects made a 10-cm reaching movement to a target placed at or near the center of the workspace, and stopped at or near the target. Reaches were in a horizontal plane, and hand trajectories were either proximal to distal and parallel to the sagittal plane, or left to right and perpendicular to the sagittal plane. Targets were placed at the center of the workspace or 5 cm to the right of center of the workspace. Before the experiment began, there was a practice session consisting of 2 blocks of 36 trials, in which the cursor was visible during the first 18 trials and no cursor was shown after movement onset in the last 18 trials. A visual cue was presented when movement time was faster than 0.7 s (solid red target) or slower than 0.9 s (solid blue target). Subjects attempted to complete the movement within the time window.

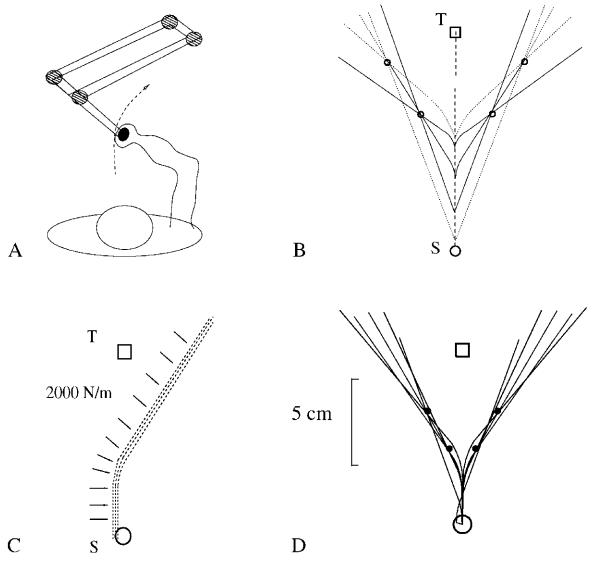

Fig. 1A–D Illustration of the experimental setup. **A** shows the subject holding the manipulandum. **C** shows the direction of forces associated with the virtual wall. **B** and **D** show the schematic and actual locations of walls used in the proximal-distal part of the reaching experiment. Starting position is indicated by *a heavy circle* and target is shown as *a heavy square*. *The small filled circles* are points at which a crossing of three walls occurs

On 60/150 randomly chosen trials, the robot enforced a position perturbation on the subject's hand trajectory which we refer to as a *virtual wall*. Subjects were instructed not to intervene voluntarily when the perturbation occurred. The virtual walls forced perturbed movements to reliably retrace the same paths so that velocity was allowed to vary, while the sequence of positions was held constant. On the remaining 90/150 trials reaching was not perturbed by the robot. The cursor was blanked out after movement onset on perturbed trials. On 60 of the unperturbed trials the cursor also disappeared after movement onset, while on the remaining trials visual cues were given as during initial training. Only trials without visual feedback of the cursor were recorded.

All five subjects completed the experimental protocol involving proximal-distal reaching movements to the center of the workspace.

Of the five subjects, subjects 3 and 4 also completed revised protocols, which involved reaching movements to a target displaced 5 cm to the right of the center of the workspace. There were two revised protocols, one with proximal-distal reaching, and the other involving left to right reaching with the virtual wall positions analogously transformed to permit comparison of the effects of different movement contexts on measured impedances.

Description of perturbations

Virtual walls consisted of two rectilinear surfaces intersecting at a small angle (Fig. 1B–D) smoothly joined by a segment of circular arc (r=4.0 cm). The first portion (1–3 cm) was nearly parallel to the line from start to target, so that significant forces were exerted mainly over the curved and second linear portions. Nominal stiffness to normal penetration was 2×10^3 N/m. Sampling rate and refresh rate for the wall forces was 100 Hz. Wall forces were always turned off 1.6 s after tone offset. Position of the manipulandum handle and force on the handle sensor were recorded for 2.2 s on each trial.

Contact instabilities (Colgate and Hogan 1989) were controlled by adding a large internal viscosity for velocities normal to the surface and dynamically altering the radius of curvature in the curved region as significant forces developed. The radius of curvature of the circular region shrank/grew at a rate proportional to normal inward/outward velocity of the hand into the wall, without changing the depth-versus-force profile of the wall at the point of contact.

The depth-versus-force profile of the wall is the relationship between the amount of penetration into the wall, and the opposing force provided by the virtual wall simulation. For large penetrations (>7 mm), this was given by the nominal stiffness 2×10^3 N/m. To avoid abrupt impacts and oscillation at the interface, a cubic profile was used within the first few millimeters which multiplied the opposing force by $(kd)^3/(1+(kd)^3)$ where d was the normal penetration in millimeters and k=8/30 was chosen to provide about 6.6 N opposition to a 5-mm penetration and about 13.3 N opposition to a 7.5-mm penetration. The force vs depth profile was kept constant because otherwise the wall would not have simulated a smooth and homogeneous surface. With appropriate tuning of parameters, this scheme conferred stability but did not appreciably alter wall locations. Subjects perceived the virtual walls as smooth, relatively rigid surfaces.

A net variation in the radius of curvature could potentially have altered the wall positions so that they were different on each trial. However, by construction the rate of change of radius of curvature depended on normal velocity, so that the net effect on the radius of curvature was proportional to the time integral of normal velocity, which is penetration distance. Therefore any net change in radius of curvature was proportional to the net change in normal penetration distance over the 2- to 4-cm curved region. If normal penetration began at a steady value when it entered the curved region and returned to the same value before leaving the curved region, the net effect on the radius of curvature would have been zero. Inspection of the data suggested that this was the case. As long as several conditions do not collapse into one, movement of the walls does not matter because the exerted torques would have been estimated in the same way.

There were ten virtual walls with deviation angles ranging from ±20.0 degrees to ±40 degrees. The walls were arranged in four triply crossed configurations as shown schematically in Fig. 1D, with two such configurations each placed to the left and right of the target, with the middle (30 degree) wall of the triple in common. Each perturbation was replicated 5 times in the course of the experiment except for the ±30-degree perturbations, which were replicated 10 times, being common to two triples. The angles, locations, stiffnesses and viscosities of the walls were chosen by trial and error to ensure firm and continuous contact with the virtual wall throughout the majority of the perturbed movement. The system of virtual walls shown in Fig. 1D has been adjusted from the idealized version shown in Fig. 1B to minimize anomalies such as bounces at initial contact, and to compensate for asymmetrical penetration of the walls on the right and left.

The triple crossing pattern was chosen to simplify a theoretical lower bound for the number of parameters which could be estimated near the crossing point P for a single replication (one trial per wall). While we did not specifically estimate parameters at the crossing points, the associated reasoning provides a lower bound for the overall number of parameters which could be estimated.

At a minimum, it is desirable to estimate ten independent parameters per replication near each crossing point P, including two constants, four parameters from the stiffness matrix and four parameters from the viscosity matrix. Therefore at least ten independent equations are needed near P. At the crossing of two walls there are 2×2=4 equations expressing force components in x and y as combinations of the parameters and four more equations are obtained by taking neighboring points on the two walls. Additional neighboring points on these lines would be collinear and would not give new equations. Thus where two walls cross there are only 4+4=8 equations to determine 10 parameters in a single replication at P. By contrast, there are 6 equations at a triple crossing point and 3×2=6 more can be obtained from neighboring points on the lines.

Theory: identification of forces

This paper presents both measurements of stiffness and simulations of trajectories based on these measurements. The present section details the relationship between the forces measured during motion, the stiffness and viscosity parameters, and the control schemes to be simulated. The arm angles at the shoulder and elbow are denoted by $q(t)=(q_1(t),q_2(t))$.

The objective of the experiments reported here is to determine how the torque α exerted by the arm depends on $q(t)$, $\dot{q}(t)$ and time t during movement. In Appendix A, it is shown that it is reasonable to assume a linear model for position and velocity-dependent restoring forces. Specifically, we will assume that near $q_a(t)$ the torque exerted by the arm muscles is

$$\alpha(t) = K(t)(q(t) - q_a(t)) + B(t)(\dot{q}(t) - \dot{q}_a(t)) + f(t) \quad (1)$$

where the first two terms represent the restoring torques due to the stiffness and viscosity of the arm respectively, and the last term $f(t)$ is discussed further below.

In practice, stiffness is measured by pushing the trajectory away from its unperturbed path $q_a(t)$ to a perturbed path $q(t)$, and expressing the position-dependent restoring force as a linear function of $q_e(t)=q(t)-q_a(t)$. However, the contributions of other forces, including viscous and inertial forces, must be accounted for in order to isolate the position-dependent force exerted by the arm. Suppose that the torque exerted by the arm muscles is $\alpha(t)$ and the perturbation torque is $r(t)$. Then the motion of the arm $q(t)$ arises from the difference of $\alpha(t)$ and $r(t)$ as summarized by the equation:

$$D(q(t),\dot{q}(t),\ddot{q}(t)) = \alpha(q(t),\dot{q}(t)) - r(t), \quad (2)$$

where D ($q(t)$, $\dot{q}(t)$, $\ddot{q}(t)$) represents the inertial torques (torques proportional to the segment masses) on the trajectory $q(t)$ for a two-jointed arm. Equation 2 indicates that, as might be expected, the perturbation torque $r(t)$ is balanced by both α and inertial contributions to the overall torque.

With the above definitions, the torques $f(t)$ are those necessary to drive the arm along $q_a(t)$. This follows because on the unperturbed path $q_a(t)$, the perturbation torque $r(t)$ is zero and Eq. 2 simplifies to:

$$D(q_a(t),\dot{q}_a(t),\ddot{q}_a(t)) = \alpha(q_a(t),\dot{q}_a(t)) = f(t) \quad (3)$$

The right-hand side of Eq. 3 is equal to $f(t)$ since the equality $q(t)=q_a(t)$ holds in the first two terms of the expression for α in Eq. 1 above. This means that $f(t)$ is the torque which produces $q_a(t)$ exactly when applied to the inertial arm.

By combining Eqs. 2 and 3, the restoring torques proportional to the coefficients $K(t)$ and $B(t)$ may be isolated from the inertial torques. Subtracting Eq. 3 from Eq. 2 gives the equation:

$$D(q(t),\dot{q}(t),\ddot{q}(t)) - D(q_a(t),\dot{q}_a(t),\ddot{q}_a(t)) = K(t)(q(t)-q_a(t)) + B(t)(\dot{q}(t)-\dot{q}_a(t)) - r(t), \quad (4)$$

so that the model components $K(t)\ (q(t)-q_a(t))+B(t)\ (\dot{q}(t)-\dot{q}_a(t))$ can be fitted to the sum of $r(t)$ and the inertial torque difference on the left-hand side of Eq. 4. No other terms proportional to $\ddot{q}(t)$ need to be considered in estimating α.

The assumption that α contains no explicit dependence on the angular accelerations can be justified as follows. There is no physiological mechanism available to significantly alter the mass or shape of the limb segments. Hence terms of the form $I(t)\ddot{q}(t)$, where $I(t)$ is an inertia, are adequately accounted for in the inertial equations of motion. Since no evidence of explicit torque feedback based on $\ddot{q}$ has previously been presented, it is a reasonable simplification to assume that exerted forces balancing the inertial forces are purely time-dependent torques delivered as $f(t)$. This is comparable to the approach of Hodgson and Hogan (1999) and Shadmehr and Mussa-Ivaldi (1994).

In Appendix A, it is shown that Eq. 4 is an effective approximation to the restoring torque even when the exerted arm torque α is a non-linear function of q provided $q(t)$ is close to $q_a(t)$. Specifically, the right-hand side of Eq. 4 is the second term in the series derived in Appendix A, and the expression for α is the sum of the first two terms. When the perturbation is not small, forces must be derived from or fitted to a fully non-linear model. A more detailed account of the relationship between experimentally observed and perturbation forces is given in Appendix B.

Bootstrap variance estimates

Many conventional statistical tests use a specific assumption (such as normality with mean zero) and mathematically deduce the expected properties of a sample of N observations from this assumption. It is then possible to see which sample results would be common under the original assumption, and which would be rare. If the experimentally obtained result would have been unlikely, it tends to refute the assumption.

Bootstrapping (Davison and Hinckley 1997) is a simulation technique which can be used when it is not clear what specific distributional assumption is appropriate. In this approach, the original data are taken as representative of the (possibly shifted) parent distribution, and a large number of artificial samples are generated. Thus, the sampling distribution is derived by simulation rather than mathematical deduction. This sampling distribution is used as a conventional sampling distribution would have been used to decide whether the certain sample outcomes (such as zero mean) would be common or rare given the parent distribution.

Several of the stiffness parameters which were estimated are non-linear functions of the data, or covary with a large number of other parameters, complicating the interpretation of statistics based on the normal distribution. Thus, we computed estimates of parameter variability using bootstrap estimates (Davison and Hinckley 1997) which produce distribution free estimates of variability. The confidence limits presented in the figures were computed by simulating 1000 replications of the experiment using stratified random sampling with replacement within each perturbation condition. This was performed for each subject. The upper and lower limits of the quantity of interest were taken as the simulated observations ranked 975th and 25th respectively. These confidence intervals were in general agreement with confidence intervals computed using a less computationally demanding jackknife estimate, which was used in exploratory analyses. To perform the jackknife, a single observation was successively deleted from each perturbed condition to yield five experimental replications with four trials per condition. The population standard deviation was then estimated from the variation among the subsets, after correcting for the fact that the subsets were not independent (Davison and Hinckley 1997) and the resulting standard deviation was used to compute a conventional confidence interval based on a t-statistic.

Simulations

Simulations were programmed in C under a Linux operating system and controlled using a custom built X-Windows interface. The equations of motion of a two-link arm model (Spong and Vidyasagar 1989) with parameters derived from measurement of the subject's arm (McConville et al. 1980) were integrated using a Runge-Kutta-Fehlberg method (Forsythe 1977), where controlling torques satisfied the assumptions of models described in the text.

Arm simulations were modified to account for the viscous and inertial load due to the robot arm during movements which were otherwise unperturbed. We modeled properties of the unpowered manipulandum by using the equations of motion for a two-link robot with known inertias, and fitting a simple model of the non-inertial torques as it moved freely in different parts of the workspace after a brief torque pulse. It appeared that at angular velocities similar to those which occurred during an unperturbed reach (approximately 0.13 rad/s at the manipulandum "shoulder," and 0.44 rad/s at the manipulandum "elbow") these torques were small, translating to endpoint forces of <1/3 N at the speeds indicated. Since even such small forces could potentially change the final position by several centimeters during a simulated reach, non-inertial torques were modeled as a viscosity matrix:

$$\begin{bmatrix} -.37 & .2 \\ .034 & -.27 \end{bmatrix}$$

(N m s/rad) in simulations of the arm and manipulandum compound object.

Results

Forces during reaching

Figure 2 illustrates the average forces observed during 10-cm reaches to a target position 5 cm to the right of the workspace center in subject 3. Figure 2A shows a 10-cm reach from left to right, while Fig. 2B shows a 10-cm reach from proximal to distal. Forces displayed on the unperturbed reaching trajectories are the net driving forces produced by the subject's arm as a result of shoulder and elbow torques, computed by substituting the trajectory of the arm into the equations of motion. Thus the displayed forces on the unperturbed trajectories correspond to $f(t)$ in Eq. 3. The accompanying insets show force recorded at the interface between the robot and the subject's hand during virtual wall perturbations at angles 20, 30 and 40 degrees, during the 1.6 s that the walls were turned on. These results illustrate that while the forces exerted by the arm against the wall and the wall against the arm on perturbed trials cancelled one another, they were considerably larger than those required to produce unperturbed movement. These patterns are typical, and the fact that force against the wall shows little tendency to decline during the terminal phases of the perturbed movements suggests that subjects followed the instruction not to voluntarily intervene.

Variations in stiffness

We computed stiffness of the arm during different parts of the perturbed trajectory in both joint and endpoint

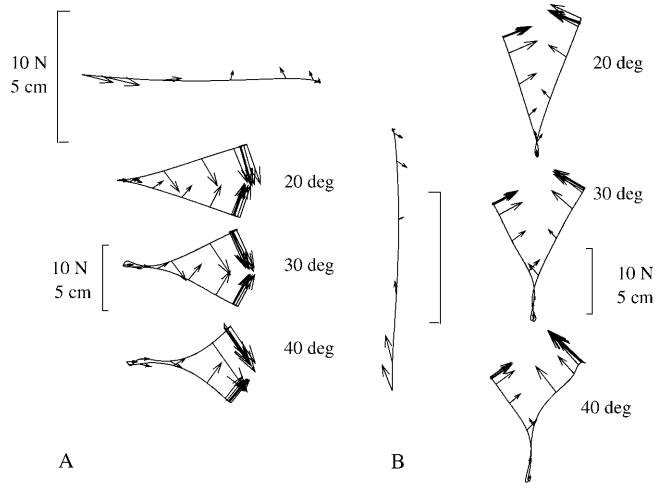

Fig. 2A, B Average forces during unperturbed and perturbed trials are shown for subject 3, with force magnitudes proportional to arrow length. *Arrows* are at 150-ms intervals. *Scale bars* each denote 5 cm, or 10 N, and indicate a magnification of 2 on the unperturbed reaching insets. *Insets from top to bottom* show average forces against the force sensor during five virtual wall perturbations at 20, 30 and 40 degrees respectively. *Top of* **A** shows average endpoint forces produced by the arm during 60 unperturbed reaching trials from left to right. *The left-hand trace of* **B** shows average forces produced during 60 unperturbed proximal-distal reaching trials, while *insets from top to bottom* show force against the force sensor during 20-, 30- and 40-degree virtual wall perturbations respectively

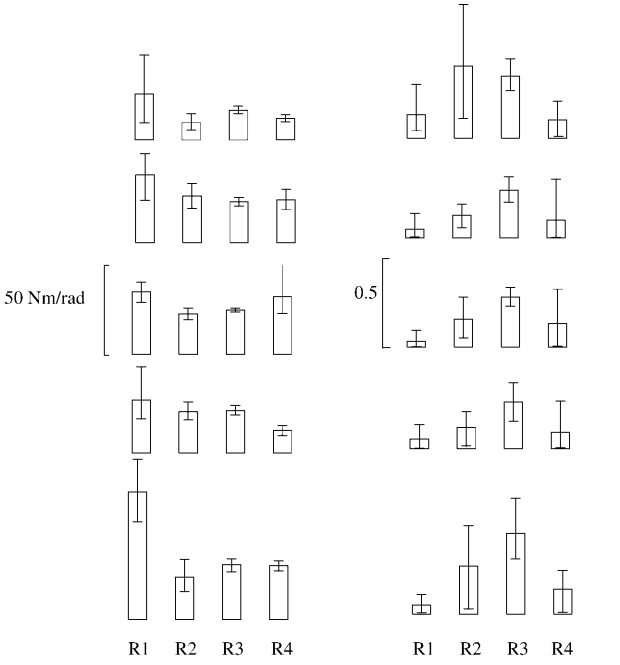

Fig. 3 *From top to bottom, the left panel* shows values of the RMS stiffness in joint coordinates for subjects 1–5 in each of the four regions, while *the right panel* shows the eigenvalue ratios. The regions R1–R4 are arranged in order of decreasing distance from the target. Confidence limit flags lacking cross bars have been truncated on the figure

coordinates in order to determine whether stiffness parameters varied reliably during movement. To do this, the plane was divided into four 2.5-cm strips which ran perpendicular to the direction of motion beginning 2.5 cm away from the starting point, ending 2.5 cm beyond the target position and labeled *R*1–*R*4. Regions were thus defined relative to movement context, but also corresponded to ranges of arm posture. Each perturbed trial generated a subset of data falling within each region. The data falling within each region were fitted to a simple model to determine arm stiffness in joint coordinates. This model was:

$$\tau = K_i(q - q_{av}) + B_i(\dot{q} - \dot{q}_{av}), \tag{5}$$

where the average of the unperturbed joint angle trajectories $q_{av}(t)$ was used to approximate q_a and K_i and B_i were constant symmetric matrices different for each subject and region i=1, 2, 3, 4 and τ were torques corrected for inertial contributions as described above. The assumption that $q_{av}(t)$ is a suitable approximation to q_a is verified by direct calculation in the section below on movement simulation. Relaxing the assumption of symmetry resulted in some additional variability, but did not affect the overall pattern of results. The eigenvalues g_1 and g_2 and eigenvectors w_1 and w_2 of K_i were calculated by standard methods, and we computed root mean square (RMS) stiffness $\upsilon = \sqrt{g_1^2 + g_2^2}$, and absolute value ratio r=$|g_2/g_1|$ where g_1>g_2. By the definition of eigenvalues, the numbers g_j,j=1,2 and vectors w_j,j=1,2 must satisfy the matrix equation $K_i w$=gw, meaning that the eigenvalue g is the scalar stiffness along w and the w_j,j=1,2 are the directions which make the restoring force direction exactly opposite to the displacement direction. The bootstrap technique was used to estimate the variability of these quantities and construct 95% confidence intervals for their values. Stiffness parameters in different regions A and B were considered different if the mean value region A fell outside of the confidence limits for region B or vice versa.

Data were not collapsed across subjects because we wanted to study the control strategies employed by each subject rather than an aggregate control strategy. Angular excursions during the proximal-distal movement were approximately 12 degrees at the shoulder and 24 degrees at the elbow. Figure 3 shows bar graphs of the RMS stiffness v, which is a measure of the overall stiffness (left panel) and eigenvalue ratio r (right panel), which is a measure of the asymmetry in the magnitudes of the eigenvalues in the stiffness matrix K_i. The RMS stiffness was larger in region *R*1 relative to other regions in three of five subjects, but otherwise exhibited no clear trend. The right-hand panel of Fig. 3 indicates there was a systematic increase in the ratios of principal stiffnesses in joint space in mid-movement (R3), but finally stiffness parameters returned to values which prevailed near the start. The eigenvalue ratio data, however, had significantly smaller values in *R*1 and/or *R*4 in every subject. Even where differences were non-significant, every subject had the same trend.

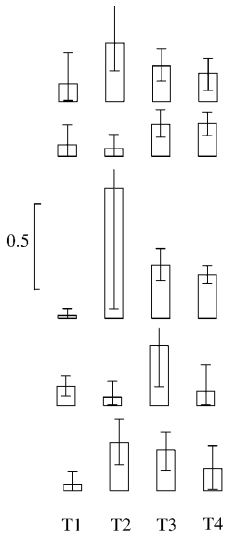

Fig. 4 *From top to bottom*, bar graphs show values of the eigenvalue ratios in joint coordinates for subjects 1–5 in each of the four time epochs, *T*1–*T*4. Each epoch was 0.2 s in duration and *T*1 begins 0.2 s after movement initiation. Confidence limit flags lacking cross bars have been truncated on the figure

These significant differences were most robust in joint coordinates, and nearly disappeared when a similar segmentation of the movement in time was examined. Figure 4 shows bar plots of the eigenvalue ratios for the joint stiffness matrix when the model is estimated with a segmentation by time into epochs *T*1=(0.2, 0.4) s, *T*2=(0.4, 0.6) s, *T*3=(0.6, 0.8) s and *T*4=(0.8, 1.0) s instead of the previous segmentation into spatial regions. Display conventions are the same as those in the right panel of Fig. 3. While the mean RMS stiffnesses (not shown) showed relatively little variation in time, it may be seen that the pattern of joint stiffness ratios over time is variable across subjects, with subjects 2, 3, and 4 showing different patterns from each other and subjects 1 and 5. A dependence on time would have suggested precise feedforward programming of impedance structure (Lacquaniti et al. 1992).

Experimental accuracy was not sufficient to provide accurate separate estimates of the four coefficients of shoulder and elbow stiffness and cross-stiffnesses across the spatially segmented analysis. However, when movements were segmented by time and the stiffness was estimated at times when unperturbed movements would have terminated (0.8–1.6 s) with the walls still present, direct shoulder stiffnesses ranged from 11.8 to 26.5 N m/rad, and elbow stiffnesses from 2.7 to 10 N m/rad. Hand velocities were typically 1–5 cm/s during this time, so that these values cannot be interpreted as postural stiffnesses.

Table 1 shows the percentages of torque variance explained by viscosity terms in a simple linear model for exerted torques in each region *R*1–*R*3. The subscripts of τ_i,*i*=1,2 refer to shoulder and elbow torques respectively. Percentages of explained variance were obtained by comparing the values of R^2 for regression of the torques on joint angles alone, with the values of R^2 for a similar regression of torques on both joint angles and joint angular velocities in each region, for each subject. Mean percentage variance explained for both τ_1 and τ_2 by angles alone

Table 1 Percentage torque variances explained by viscosity

Region	Var(τ_1) (%)	Var(τ_2) (%)	Hand speed (cm/s)
R1	0.4–7.0	8.8–12.0	15.8–19.9
R2	1.2–7.8	0.2–3.6	14.8–19.2
R3	0.6–3.8	1.2–4.8	2.2–5.6
R4	–	–	1.2–4.6

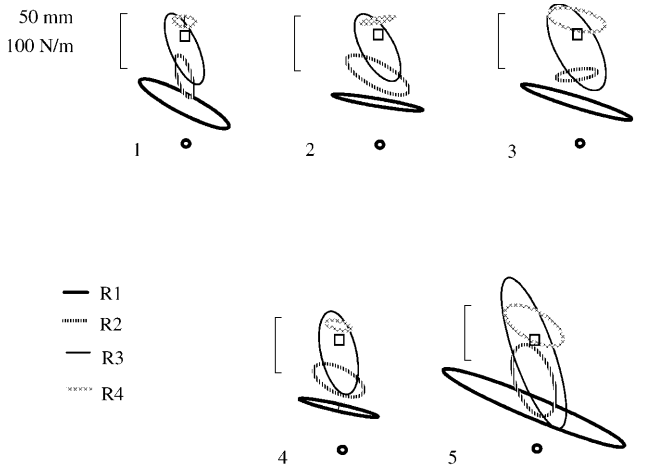

Fig. 5 Endpoint stiffness ellipses are shown in regions *R*1–*R*4 for proximal-distal reaches to the center of the workspace in all five subjects. The ellipses are computed using the jacobian of the transformation from angular to endpoint coordinates at the center of each region. Location of the movement starting point is shown as *a heavy circle*, and location of the target is shown as *a light square*

was approximately 85% (*R*=0.92) across all subjects and regions *R*1–*R*3. Data from a simple linear model with fixed intercepts are presented rather than the time-dependent symmetry-constrained model (Eq. 5) because the time dependence and non-linear fitting procedure used in the latter case to obtain symmetry would complicate the interpretation of differences in R^2. Similar viscosity patterns were found in both models, however. The small size of the torque variations explained by the viscosity terms makes them more susceptible to experimental error and to errors in the model. There was a tendency for viscous forces to have less relative importance at slower hand speeds. Many of the trajectories had nearly zero velocity and zero variation in joint angles in region *R*4, invalidating the fitting procedure in this region and leading to non-physical estimates of viscosity there. Because of the size of the obtained confidence intervals for viscosity, it was not possible to make reliable statements about variation of viscosity over space. Constant viscosity estimates in the context of a global torque model for each subject are reported below.

The variation in joint stiffness properties had consequences for the endpoint stiffnesses shown in Fig. 5, which shows endpoint stiffness ellipses for each subject during proximal-distal reaching computed in each region *R*1–*R*4 on perturbed trials. Each ellipse shows the

magnitude of the force response to a unit perturbation in endpoint position aligned with a vector from the center of the ellipse to its perimeter. As might be expected, the increase in the ratios of the principal stiffnesses in joint space (Fig. 3, right panel) gives endpoint stiffness ellipses at *R*2 and *R*3 which have less elongated shapes relative to *R*1. There is a rotation in direction of the long axes of the stiffness ellipse in endpoint space in *R*3 seen in every subject so that the long axis roughly points along the forearm. The reduction in endpoint stiffness in region *R*4 comes about because the definition of torque implies lateral endpoint stiffness decreases with increasing shoulder extension for constant shoulder stiffness. The exaggerated elongation of the *R*1 stiffness ellipse may be related to more rapid components of the response to perturbation, as hand speeds in this region were 15.8–19.9 cm/s as shown in Table 1. Stiffness ellipses had an unstable direction along the minor ellipse axes in *R*4 for subject 1 and in *R*1 for subject 4. These findings are likely due to experimental error, since the observed eigenvalues in these directions were not significantly different from stable ones.

The fact that these changes in stiffness parameters occurred primarily with spatial segmentation rather than time meant that they depended primarily on limb position. This suggests that stiffness changes depend on passive factors such as posture (Tsuji et al. 1995; Mussa-Ivaldi et al. 1985), muscle synergist load sharing (Kuo 1994) whether contraction was concentric, eccentric or isometric, or other non-linearity in the response to deviation from the reference point on the unperturbed trajectory average (Bennet et al. 1992; Bennet 1993). Since forces were mainly isometrically exerted and non-decreasing (Fig. 2), Fig. 3 provides direct evidence against a dependence on contraction type, and since the wall perturbation causes the deviation from the reference point to increase, it is unlikely that this monotonic increase alone accounts for the non-monotonic changes in stiffness parameters.

To study the relationship between stiffness variation and movement context, the variations in stiffness during a 10-cm reaching movement from left to right were also studied in subjects 3 and 4. Angular excursions during the left-right movement were approximately 10 degrees at the shoulder and 3 degrees at the elbow. The results of these analyses are shown in Fig. 6. The bar graphs show joint stiffness parameters defined as in Fig. 3, in the regions *S*1–*S*4, which are 2.5-cm strips running perpendicular to the direction of motion, starting 2.5 cm to the right of the starting point, and ending 2.5 cm beyond the target. These data show systematic trends in the RMS stiffness, which is increased in *S*3, and a systematic trend in the eigenvalue aspect ratio, which reaches a minimum in *S*3. Subject 4 has less variability than subject 3, but the overall trends are the same in each subject. The lower part of the figure shows endpoint stiffness ellipses in regions *S*1–*S*4 for subject 4. As might be expected, the decrease in the ratios of the principal stiffnesses in joint space (Fig. 6, right panel) corresponds to endpoint stiffness ellipses at *S*2 and *S*3, which have more elongated

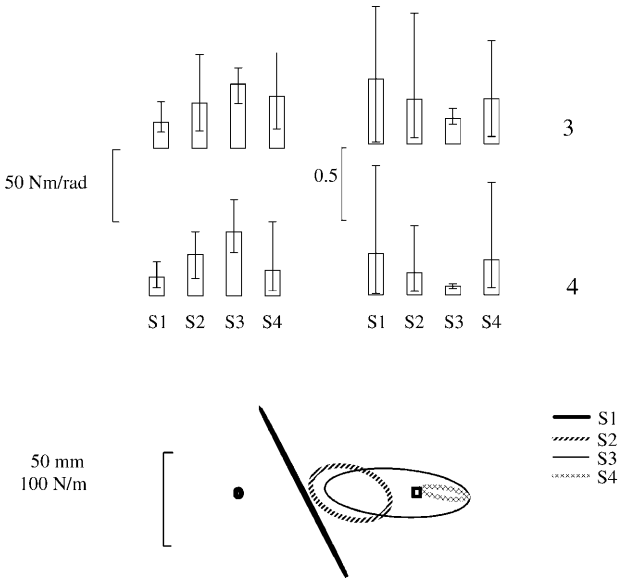

Fig. 6 *The left panel* shows values of the RMS stiffness in joint coordinates for subjects 3 and 4 in each of the four regions, *S*1–*S*4, while *the right panel* shows the eigenvalue ratios. Confidence intervals were computed and displayed as in Fig. 3. *The bottom inset* shows endpoint stiffness ellipses in regions *S*1–*S*4 for subject 4. Movement starting point and ending point are indicated as in Fig. 5

shapes relative to *S*1. It is seen that, as in the proximaldistal reach, the endpoint stiffness ellipse turns so that its major axis is more aligned along the direction of motion in *S*3. Unlike the proximal-distal movement at *R*3, this endpoint stiffness ellipse does not point along the forearm.

In the left-right movements, stiffness parameters follow a pattern of variation which is clearly different from that of the proximal-distal movement. The tendency for terminal joint stiffness parameters to resemble those near the start of movement seen in the proximal-distal reach is also seen in Fig. 6, however. While this tendency is not obvious in the endpoint stiffness ellipses, we note that some apparent variation in endpoint stiffness occurs as a result of the coordinate transformation from joint to endpoint coordinates, and not because joint stiffnesses have changed.

Taken together, the data of Figs. 3, 4, 5, and 6 suggest that the patterns of restoring force are strongly associated both with the position of the limb, and the direction and progress of movement, which interact to produce the observed patterns of stiffness. The orientation of the endpoint stiffness ellipse in *R*3 could be explained by a postural mechanism, since stiffness along the forearm direction should be greatest at a 90-degree elbow angle, where elbow joint elasticity is decoupled from that of the shoulder. In the left-right movement, a mechanism producing the observed orientation is suggested by the fact that a braking force must be generated at the elbow in the second half of movement to maintain a nearly fixed elbow angle, and this implies increased muscle activity about the elbow joint.

Restoring torque model

Since stiffness appeared to vary systematically in joint angle space during movement, and since stiffness expresses the linear relationship between torque and joint angles, we conclude that the relationship between torque and joint angles in the presence of large perturbations is nonlinear. While it is possible that some of the observed variation was due to variation in time, stiffness cannot emulate a spatial constraint unless restoring torques are functionally related to joint angle and joint angle velocity. Thus, in this section, goodness of fit of this relationship is assessed. In addition goodness of fit is compared for nonlinear functional relationships consistent with energy-conserving elastic forces, and those which are not consistent with these properties. This clarifies the possible role of postural stability mechanisms and stiffness modulation during movement, using the following reasoning.

Position-dependent (elastic) restoring torques appear to be the dominant involuntary postural stability mechanism (Mussa-Ivaldi et al. 1985). Therefore if restoring forces during motion are shown to be energy-conserving elastic forces, it is evidence that postural stability mechanisms are used during movement. By stability is meant the tendency to return to the original posture, or original trajectory after a disturbance. However, while unmodulated elastic restoring forces can make a posture return to its original value quasistatically, they cannot cause a movement trajectory to return to its original path after a disturbance. Since elastic forces do not dissipate energy, the effect of a transient disturbance will persist as a continuous oscillation unless there is a large viscosity or a (possibly voluntary) modulation of stiffness. Therefore if restoring forces during motion are shown to be energy-conserving elastic forces, it would also suggest that stiffness modulation is necessary for stability.

A potential field is the non-linear extension of a symmetric stiffness matrix, which is characteristic of postural stiffness (Mussa-Ivaldi et al. 1985). The distinguishing physical feature of such a field is that the forces produced over any exactly repeated movement can neither add nor remove energy from the system, so that it cannot drive repetitive movements which perform net work. A potential field can be expressed as the gradient or slope of a scalar function called a potential (Courant and Hilbert 1953, 1954). It can be shown that the gradient $[Q_1(q_1,q_2),Q_2(q_1,q_2)]$ of a potential function must satisfy the symmetry condition $\partial Q_1/\partial q_2=\partial Q_2/\partial q_1$ for all values of q_1 and q_2. The hypothesis that the observed torques are a potential field would be falsified if adding non-conservative terms to the regression gave significant increases in goodness of fit, or improved the ability of the fitted torque model to simulate movement. The latter possibility is investigated in a later section.

We fitted non-linear joint-angle relationships to the torque data of the form:

$$\begin{bmatrix}\tau_1\\ \tau_2\end{bmatrix}=\begin{bmatrix}Q_1(q_1,q_2)\\ Q_2(q_1,q_2)\end{bmatrix}+B\begin{bmatrix}\dot{q}_1\\ \dot{q}_2\end{bmatrix} \quad (6)$$

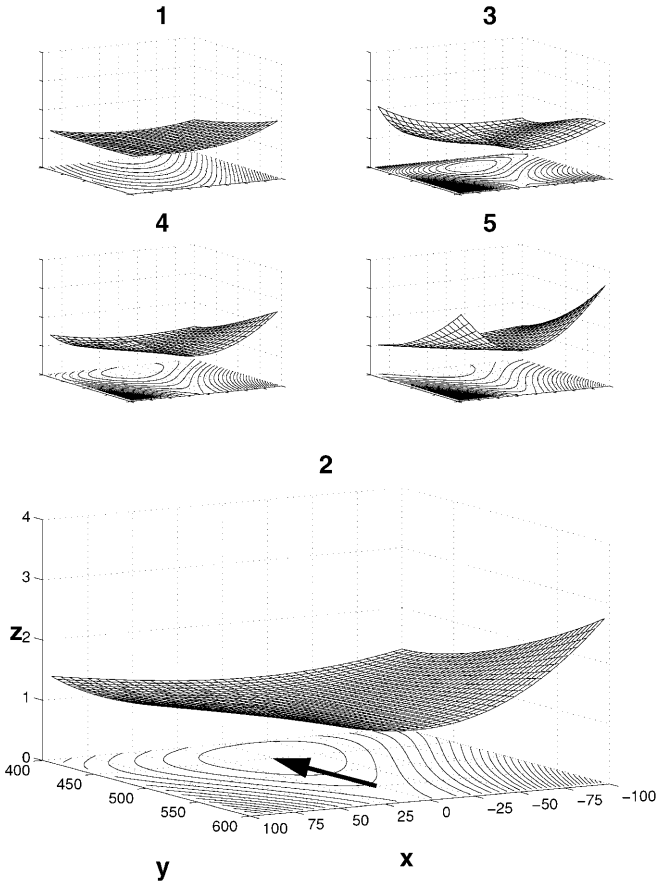

Fig. 7 Inverted three-dimensional perspective plots of the force/torque potential functions for each subject are shown in cartesian coordinates. When forces are represented as the gradient of a potential function, the same scalar function which represents the relationship between joint angles and torques also represents the relationship between cartesian coordinates and endpoint forces. Lines of equal surface height (contour lines) are shown on the *xy*-coordinate plane, while *the arrow on the bottom inset* shows direction and extent of the proximal-distal reaching movement studied

where τ_1 and τ_2 are the torques at the shoulder and elbow, $Q_1(q_1,q_2)$ and $Q_2(q_1,q_2)$ are polynomials of order less than 3, in the joint angles q_1 and q_2, and B is not constrained to be symmetric. In order that the first term of Eq. 6 represents a conservative force field, the partial derivatives of $Q_1(.,.)$ and $Q_2(.,.)$ have to satisfy the symmetry condition. The models were fitted to an initial period of the perturbed trials equal to the median time to reach the furthest extent of the movement, for each subject (range 0.66–0.8 s). Once the coefficients in Eq. 6 had been estimated, for $Q_1(.,.)$ and $Q_2(.,.)$ satisfying the consistency condition, the scalar potential could be obtained by direct calculation.

Scalar potential functions for the estimated torque fields for proximal-distal reaches for each subject are shown in Fig. 7. These polynomials contained only terms $a_{mn}q_1{}^nq_2{}^m$, $m+n\leq 2$, and satisfied the consistency conditions, thus specifying a model containing 12 parameters when B is included. Correlations between data and the fitted

Table 2 Constant viscosity estimates in potential model

Subject ID	(N m/rad/s) b_{11} b_{21}	(N m/rad/s) b_{12} b_{22}
1	–2.1±0.22 –0.86±0.16	–0.84±0.15 –0.78±0.14
2	–1.2±0.23 –0.38±0.17	–0.097±0.16 –0.44±0.14
3	–1.25±0.24 –0.18±0.18	0.075±0.17 –0.50±0.15
4	–1.33±0.23 0.05±0.17	–0.076±0.17 –0.47±0.15
5	–2.5±0.39 0.32±0.31	0.14±0.26 –0.14±0.24

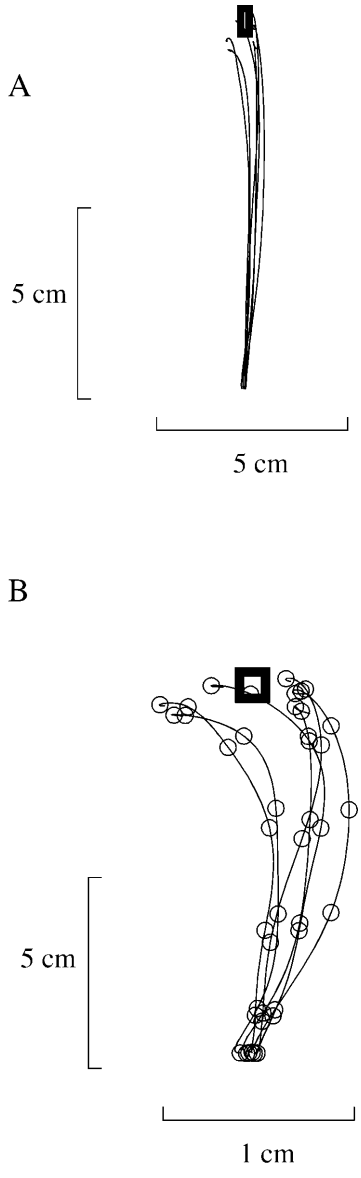

Fig. 8A, B Six proximal-distal reaching trajectories for subject 3 are shown. The position of the target is indicated by *the heavy square*. **A** shows the reaching trajectories as *thin lines* with an undistorted scale. In **B** symbols on the traces appear every 150 ms and the scale is expanded five-fold in the *x*-direction to show lateral variation in the trajectory more clearly

polynomials ranged from 0.93 to 0.96 for proximal-distal reaches and 0.91 to 0.95 for left-right reaches (left-right functions are not shown), and individual *t*-statistics for the non-linear terms in the regression were always statistically significant. Of the five subjects, three showed clear minima near the target, while for the remaining two the target lay in a valley of the surface but there was no minimum in the region shown. This suggests that such potential surfaces do not completely define the restoring force model, and that viscous and time-dependent factors may also be important. It should be noted that if stiffness and viscosity matrices were constant, this situation would also lead to a simple conservative non-linear potential.

Table 2 shows the constant estimates of joint viscosity during movement for the potential model, together with 95% confidence intervals derived from the theory of multiple linear regression (Johnson and Wichern 1988). Indices of the table entries b_{ij}, i=1, 2 and j=1, 2 refer to shoulder and elbow respectively. Thus b_{11} is the direct shoulder viscosity and b_{22} the direct elbow viscosity. All the mean estimates were consistent with positive damping. These estimates were most reliable for the shoulder viscosities, which varied by a factor of approximately 2 across subjects. Except for subject 1, the pattern of means and confidence intervals for cross viscosities (off-diagonal terms) does not suggest a systematic deviation from zero. Excluding subject 5, the mean direct elbow viscosities were significantly different from zero and vary by a factor of approximately 2 across subjects. For subject 5, the direct elbow viscosity is of the correct sign but is not significantly different from zero. The findings for subjects 1 and 5 may have occurred because of differences in strategy employed by these subjects, and/or because the torque model was a simplified description of the systematic features of generated torques. Tsuji et al. (1995) found a similar pattern of joint viscosities during posture, but their viscosity estimates were about half the size of the present estimates during movement.

For comparison, a second polynomial model was fitted (Eq. 6) in which $Q_i(q_1,q_2)$ contained all terms of the form $a_{ik}q_i^k$, i=1, 2; k=0, 1, 2, 3 and coefficients were not forced to satisfy the consistency condition. Since the resulting field is non-conservative, it could not be represented as a potential function and is not shown. This model contains 16 parameters when B is included. Correlations were only slightly larger for each subject (for proximal-distal reaches 0.95–0.97 vs 0.93–0.96) than those achieved for the conservative model, which had fewer parameters. These results establish that observed torques are consistent with a single non-linear restoring force model based on joint angles. No clear difference in the goodness of fit between conservative and non-conservative models was seen, however. Comparison of the ability of these models to simulate movement is given below.

Attractor and movement simulations

To determine whether the observed patterns of stiffness were consistent with a role in constraining movement, a

number of simulation studies were performed. The trajectories of six typical unperturbed proximal-distal reaches for subject 3 are shown in Fig. 8A, B for comparison with simulation results. The trajectories are scattered over an approximately 1-cm range near the target. Presumably such variation is due to noise in both planning and execution of movement. However, a constraint model attributes error chiefly to execution errors in a single intended movement, which was modeled previously by the mean movement.

The global torque model implies that there is a nominal trajectory $q_a(t)$ which is called the attractor trajectory. With some assumptions this attractor trajectory can be computed from Eqs. 1 and 2 for each trial. The properties of these computed trajectories provide a test of the hypothesis that the global torque model constrains movement.

If constraint based on stiffness is important in correcting small errors in the trajectory, two conditions on the attractor trajectories have to be satisfied. First, the attractor trajectories should not be much more variable than the observed trajectories. If the model implied that extreme attractor trajectories are necessary to explain the variation in the observed trajectories, then the attractor trajectories must depend systematically on the exerted torque for each trial. Such dependence is inconsistent with a constraint model because a constraint based on the mechanical state of the arm cannot require any knowledge of the specific error which is going to occur. Second, the individual reference trajectories must be significantly different from the actual trajectories. Perfect identity of individually observed and attractor trajectories would suggest equilibrium point control rather than constraint because it would suggest that each trial has a different desired trajectory. Thus two tests of the constraint model can be performed by simulating the attractor trajectories for each trial. To compute the attractor trajectories, the linear control scheme of Eqs. 1 and 2 was algebraically solved for $\dot{q}_a(t)$ to obtain a differential equation. The resulting expression for $\dot{q}_a(t)$:

$$\dot{q}_a = \dot{q} + B^{-1}K(q - q_a) - B^{-1}(\tau - f(t)), \qquad (7)$$

specifies an inverse problem for $q_a(t)$. The inertial torques τ and $q(t)$ were estimated from each observed trajectory. The model was individualized for each subject. The attractor trajectory $q_a(t)$ was computed for each trial and each subject, provided that the inverse of B was accurate and the solution for q_a was stable. The function $f(t)$ was taken equal to the average torque at time t over all unperturbed reaches, since this choice minimizes the average squared difference between τ and $f(t)$, and so is a reasonable estimate of the output of a dynamical model. The quantity $\tau=\tau(t)$ was estimated from the data for each trajectory using the method of Appendix B. Two types of estimate of the stiffness and viscosity were used. These conditions were simulated in order to evaluate the functional significance of observed variations in the stiffness displayed in Figs. 3, 4, 5, and 6. First, we employed

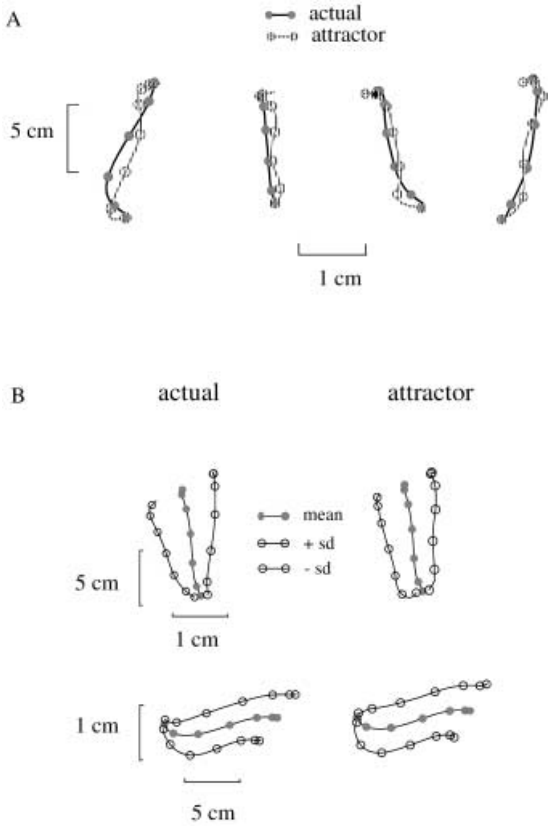

Fig. 9 **A** Reaching trajectories (*solid circles*) and computed attractors (*open circles*) are shown for the 15th, 25th, 35th and 45th unperturbed reaching trials for subject 4. The scale is expanded by a factor of 5 in the *x*-direction to show lateral variation in the trajectory more clearly. **B** The mean position (*solid circles*) and mean with the standard deviation added and subtracted (*open circles*) are shown for proximal-distal (*top*) and left-right reaches. The scale is expanded in the *x*-direction for the proximal-distal reaches and in the *y*-direction for the left-right reaches by a factor of 5

constant estimates of stiffness K and viscosity B. A second approach was to use values of $K(t)$ and $B(t)$ from the linear control scheme of Eq. 1 based on the variational equation of the polynomial model. These were derived from the polynomial models shown in Fig. 7 using the methods of Appendix A. The attractor trajectory $q_a(t)$ was computed from each unperturbed reaching trajectory by solving Eq. 7.

Figure 9A shows the unperturbed and corresponding attractor trajectories for four typical trials from a single subject using constant K and B. It is seen that the computed attractors stay within a few millimeters of the unperturbed reaching trajectories but vary apparently randomly about the actual reaches. Figure 9B shows that there was little difference between the mean and standard deviation of the 60 attractor trajectories and unperturbed reaches for the same subject. This close correspondence held for all the subjects, whether the attractors were calculated using constant K and B or coefficients derived from the conservative polynomial model as described.

The difference between attractor and actual trajectories was examined for each subject over proximal-distal

Table 3 RMS difference between the attractor and unperturbed trajectories (mm)

Model	Subject				
	1	2	3	4	5
Constant (mm)	n/a	5.2	2.4	5.8	3.4
Conservative polynomial (mm)	11.1	11.0	10.4	5.8	6.0

reaches. The root mean square (RMS) differences between 60 computed attractors and the actual trajectories for 60 proximal-distal unperturbed reaches over the first 1.0 s of each reach are given in Table 3. This RMS distance includes distance in both *X* and *Y* directions, and thus also summarizes discrepancies in timing. These variations were not due to noise in the observed torques since it was possible to reconstruct unperturbed movements from the observed torques using the dynamical equations with a high degree of accuracy. Attractors for subject 1 were computed using *K* and *B* from the polynomial model only, because computation of the attractors using constant *K* and *B* gave unstable results. In addition, the polynomial model calculation became unstable for 8/60 trials in subject 3 and 6/60 trials in subject 4 for the polynomial model. These relatively rare anomalies in the inverse computation do not cause difficulty with the model, because the motor system begins with q_a and does not have to solve Eq. 7 to obtain it.

Since the overall distance of the reach was 100 mm, the small errors in Table 3 indicate that a linear model of restoring force is sufficient to reconstruct attractor trajectories. Larger RMS discrepancies for the polynomial model reflect the lower stiffness estimates obtained in some parts of the movement when fitted stiffness is allowed to vary, and do not correspond to goodness of fit. Since the kinematics of computed attractors appear to match unperturbed movements, q_a was estimated as the average of the unperturbed reaches in what follows.

Finally, we investigated whether the values of $K(t)$ and $B(t)$ estimated from the data were of the correct structure and magnitude to provide robust control of voluntary movement. According to Eq. 1, the torque applied to the arm consists of $f(t)$ added to the torques proportional to $K(t)$ and $B(t)$. Therefore if movement could still occur when the torques $f(t)$ associated with an inverse dynamical model were absent, this would show that torques proportional to $K(t)$ and $B(t)$ are sufficient to control movement. If control of movement does not depend on an accurate $f(t)$, this would show that a movement execution strategy based on an appropriate selection of mechanical states of the arm can dramatically reduce accuracy requirements in an inverse dynamical model. To test this hypothesis, we set the driving force $f(t)$ equal to zero in the simulation. This was tested using both the conservative and non-conservative polynomial models of the restoring torque. Since the underlying models do not contain $f(t)$, it is not expected that these simulations would closely replicate unperturbed movement. However,

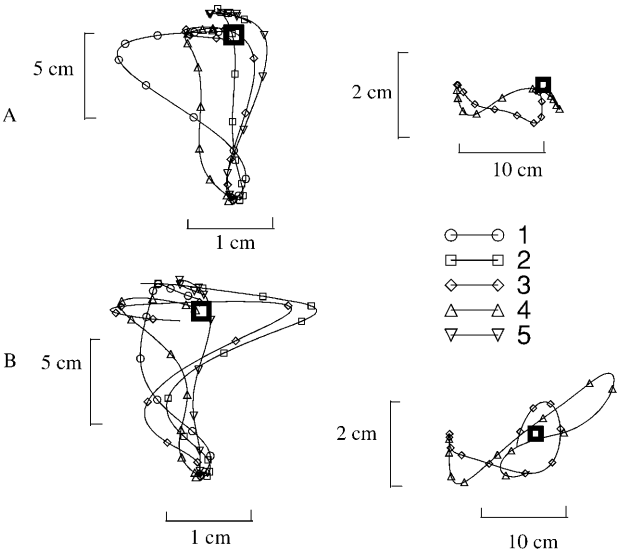

Fig. 10 Simulations of 1.6 s of unperturbed movement are shown for each subject using the linear control schemes derived from conservative **(A)** and non-conservative **(B)** models. *The left panels* show simulations of proximal-distal reaching and *the right panels* show left-right reaching simulations scaled by a factor of 2. The scales are magnified fivefold perpendicular to movement direction to show deviations from straight line movement. *The symbols* are 150 ms apart, *the legend* indicates the subject parameter set used in each simulation, and the position of the target is indicated by *a heavy square*

the clear qualitative failure of one of the conservative or the non-conservative models to produce stable movement would suggest that the mechanism it is based on is incorrect.

Simulation results are shown in Fig. 10. Linear control schemes associated with either conservative or non-conservative models were able to support stable movement simulations for all subjects in all cases except for left-right movement in the non-conservative model. It can be deduced from the spacing of the symbols that movement initiation was delayed by approximately 150 ms, probably as a consequence of setting $f(t)=0$. Detailed comparison of the simulations suggests that despite slightly lower *R* values in fitting restoring torques, the conservative model is more effective in reproducing the tendency of unperturbed proximal-distal reaches to curve counterclockwise (Fig. 8), and that the conservative model produces fewer anomalous trajectories (1/5 vs 3/5). The dramatic instability of the left-right simulation for the non-conservative model is associated with a relatively poor fit for the shoulder torques (R=0.69–0.72). The simulations for the anomalous trajectories in the non-conservative model were also performed with the viscosity coefficients replaced by those from the conservative model (Table 2) with similar results. This demonstrated that the anomalies were due to the model for stiffness and were not an indirect effect of viscosity.

While the initial delay of movement in these simulations implies a velocity profile different from unperturbed movement, the effectiveness of this control

scheme demonstrates that forces of constraint are large enough to enforce nearly normal movement even when driving forces are inaccurate.

Discussion

Our results demonstrate that stiffness varies during multijoint movement, and does so in a manner which is not simply predictable from posture, muscle contraction type, or the parameters of the experiment (Figs. 3, 4, 5, 6). Our results on stiffness modulation are generally consistent with observations by Gomi and Osu (1998), who found that viscoelastic properties of the multijointed arm can be modulated under different loading conditions. Comparison of Fig. 5 with the work Mussa-Ivaldi et al. (1985) and Tsuji et al. (1995) suggests that variations in stiffness observed in these 10-cm movements cannot be explained by variations in posture. Since the deviation from the reference point on $q_a(t)$ was monotonically growing, and stiffness parameters were not monotonically growing, stiffness variation cannot be explained by the size of the deviation from the reference point. It is possible that different stiffnesses are associated with muscles which are contracting isometrically, concentrically or eccentrically; however, as Fig. 2 shows, force generation during motion involved largely isometric or slightly eccentric contraction during perturbed trials.

Some stiffnesses we measured during movement are a factor of 1–2 smaller than those measured by Mussa-Ivaldi et al. (1985) and by Tsuji et al. (1995) during posture. However, the values observed were similar to estimates by others (Bennet et al. 1992; Bennet 1994; Gomi and Kawato 1996) who measured stiffness during movement. For example, Gomi and Kawato report an elbow stiffness range of 5–21 N m/rad over three subjects, while we found 2.7–10.0 N m/rad over five subjects near movement termination.

Stiffness magnitudes observed at other points in the movement were similar to those observed during measurements of postural stiffness (Mussa-Ivaldi et al. 1985; Tsuji et al. 1995). It is possible that these larger values of observed stiffness were related to our use of a large slow experimental perturbation. In the proximal-distal reaching experiment, of 20 conditions (5 subjects $\times$ 4 spatial domains), 10/20 RMS stiffness estimates fell below 24.6 N m/rad. The corresponding median for the two left-right reaching experimental replications was 30.0 N m/rad. Because stiffness ellipses had aspect ratios different from 1.0, substantially higher stiffnesses could be obtained in some directions. As noted by Gomi and Kawato (1996), the observed stiffness values are not high enough to enforce an arm trajectory which preserves a substantial similarity between the virtual and actual trajectories if restoring forces depend only on a positional error (forces associated with the first term in Eq. 1). The altered velocity profile in our simulation (Fig. 10) suggests that stiffness and viscosity terms constrain but do not dictate movement trajectories. Other simulations (Katayama and Kawato 1993) which have modeled reaching as an equilibrium point trajectory enforced by position-error-dependent restoring forces suggest that stiffnesses at or below 19.5 N m/rad for the shoulder and 15 N m/rad at the elbow are insufficient to enforce similarity of actual and virtual trajectories. If cross-stiffnesses between shoulder and elbow are neglected, these values correspond to a combined RMS stiffness value of 24.6 N m/rad, so that, as noted, half the observed stiffnesses were lower than this threshold.

While the observations are not compatible with simple equilibrium point control, the constraint forces we measured can be consistently described as combinations of neurally determined force field primitives (Mussa-Ivaldi and Giszter 1992; Mussa-Ivaldi et al. 1994; Mussa-Ivaldi 1997), which form a global torque model depending on joint angles (cf. Fig. 7 and Appendix A). One contribution of the present work is to show that such a model is also equivalent to a linear model in which stiffness and viscosity may vary, with the same form hypothesized by Shadmehr and Mussa-Ivaldi (1994). This account of trajectory formation differs from that of others, e.g., Gomi and Kawato (1997), because it postulates a control scheme (Eq. 1) in which $q_a(t)$, $K(t)$, $B(t)$ and associated restoring torque terms emerge from a single global torque model. It is worth emphasizing that, unlike the virtual trajectory in the equilibrium point hypothesis, Appendix A shows that neither the attractor $q_a(t)$, nor the existence of a viscosity error term $B(t)\,(\dot{q}(t)-\dot{q}_a(t))$ requires any assumption beyond the global torque model. While the torques affected by location of $q_a(t)$ cannot be experimentally distinguished from those due to $f(t)$ in a linearized model (Hodgson and Hogan 1999), this indeterminacy is removed for sufficiently large perturbations in the non-linear models we studied, so that $q_a(t)$ is experimentally as well as theoretically well defined. In linearized form, the account presented here remains consistent with the formulations of others such as Kawato and Gomi (1993), Shadmehr and Mussa-Ivaldi (1994) and Hodgson and Hogan (1999).

Different patterns of stiffness modulation are not equivalent for control of reaching as shown by our simulations detailed in Table 3 and Fig. 10. Thus the detailed pattern of constraint forces which are implied by a global torque model cannot be neglected in accounting for multijoint movement. It is demonstrated through simulation that relatively low measured RMS stiffness values are consistent with robust movement control when observed stiffness modulation patterns prevail. A limitation of the present study is that we do not establish whether the observed variations in stiffness are functionally essential to movement or controlled independently of the activation which produces $f(t)$. In addition, the present results were obtained with relatively small and slow movements and may be specific to such movements. It cannot be ruled out that subjects intervened voluntarily to some extent in responding to the wall perturbation. However, since there were ten conditions presented in an unpredictable manner, and subjects did not have visual

feedback, it appears unlikely that the consistent responses observed were a product of voluntary intervention.

The fact that restoring forces can be accounted for by energetically passive mechanisms suggests that reflex mechanisms and sensory feedback might act only to shape energetically passive mechanical properties of muscles and, thus, the mechanical state of the arm (Hogan 1985; Houk and Rymer 1981). The hypothesis that postural mechanisms continue to influence stiffness during movement remains consistent with the possibility that limb impedance is adjusted in an appropriate manner for each movement. In particular, the observed complex joint-angle-dependent variation in stiffness may occur because redundant synergist muscles which exert their influence in different pulling directions attain a varying degree of mechanical advantage at different points during the perturbed motion (Kuo 1994). Such an account might reconcile complicated observed patterns of stiffness modulation with relatively simple neural strategies for tuning joint stiffness. Further studies of muscle activation would be required to substantiate this hypothesis.

Acknowledgements This study was supported by the National Institute of Neurological Disorders and Stroke Grant NS-35673-01. I am grateful for the support of Dr. F.A. Mussa-Ivaldi, and for the comments of J. Dingwell, T. Milner, J. Patton, F. Popescu, D. Roberson, and J. Stevens, who critically reviewed earlier drafts of the manuscript.

Appendix A

In the experiments reported here, the robot enforced a relatively large lateral deviation of 1–5 cm. The data suggest that the restoring forces associated with these deviations can be described by a non-linear model which is a function of joint angle and angular velocities. In this appendix it is shown that such a global torque model implementing a spatial constraint can be equivalent to a selection of mechanical states in considering small disturbances near the intended trajectory. This derivation does not address the origin of the global model, which might arise from neural and/or biomechanical mechanisms.

In unperturbed movement, deviations about the average trajectory are small, on the order of 1 cm. We can define the dimensionless parameter ε to be the ratio of the average deviation of the path at the target across many perturbations to the entire path length, and write any disturbing force as ε $d(t)$. Thus a typical value of ε=1 cm/10 cm. While the calculation below can be done whether epsilon is small or not, the effectiveness of the approximation will vary with the size of epsilon and the physical properties of the model. The perturbation can be considered to be "small" when only a small deviation is induced in the trajectory.

A global model of torque leads to the dynamical equation:

$$D(q,\dot{q},\ddot{q}) = S(q) + B(q)\dot{q} + \varepsilon P(t) \tag{8}$$

where $q=(q_1,q_2)$ are the shoulder and elbow angles in the plane, D describes the passive dynamics of the arm, $S(q)$ gives torque as a function of q, $B(q)$ is a matrix of the form $\partial\nabla\rho(q)/\partial(q_1,q_2)$ for some scalar function $\rho(q)$, $P(t)=J^t d(t)$, and ε is the small dimensionless parameter described above. The terms on the right-hand side of Eq. 8 represent the active controller for the arm. The particular forms chosen for S and ρ do not affect the argument and more details about the choices made appear below.

Perturbation analysis is a classical technique of mathematical physics (Courant and Hilbert 1953, 1954), which has also been applied to the control of robot manipulators (Lee and Chung 1984). We assume that this dynamical equation produces a solution $q(t,\varepsilon)$, which is infinitely differentiable in t and ε. Hence it has a taylor series in ε, which we write (absorbing the factorials into the definitions of V_i, i=0, 1, 2,...) as:

$$q(t,\varepsilon) = V_0(t) + \varepsilon V_1(t) + \varepsilon^2 V_2(t)\ldots \tag{9}$$

where $V_i(t)$ are to be determined from the dynamical equation. It may be verified from Eq. 9 that $V_0(t)$ is obtained by setting ε=0 and $V_1(t)$ is obtained by computing $\partial q/\partial\varepsilon|_{\varepsilon=0}$. This procedure may also be followed to obtain the $V_i(t)$ implicitly from Eq. 8 as we now describe for $V_0(t)$ and $V_1(t)$.

Substitution of Eq. 9 into Eq. 8 yields (omitting the t arguments for brevity):

$$\begin{aligned} &D\left(V_0+\varepsilon V_1+\ldots,\dot{V}_0+\varepsilon\dot{V}_1+\ldots,\ddot{V}_0+\varepsilon\ddot{V}_1+\ldots\right)\\ &= S(V_0+\varepsilon V_1+\ldots)+B(V_0+\varepsilon V_1+\ldots)\left\{\dot{V}_0+\varepsilon\dot{V}_1+\ldots\right\}+\varepsilon P \end{aligned} \tag{10}$$

Setting ε=0 gives the equation for the unperturbed trajectory:

$$D\left(V_0,\dot{V}_0,\ddot{V}_0\right) = S(V_0) + B(V_0)\dot{V}_0 \tag{11}$$

The trajectory $V_0(t)$ corresponds to $q_a(t)$ in the text. This equation involves forces which are not accessible to experimental measurement because by definition no experimental perturbation has been given. While it is possible to deduce the net torques as a function of time using the passive dynamical equation of the arm, not much can be determined about their space or velocity dependence without perturbing the arm.

To determine the equation satisfied by $V_1(t)$, we differentiate both sides of Eq. 10 with respect to ε and then set ε=0, which removes the non-linear terms. In this manner, using the product rule on the term involving $B(q)\dot{q}$ in Eq. 8 we obtain:

$$\begin{aligned} &[D_1]V_1 + [D_2]\dot{V}_1 + [D_3]\ddot{V}_1\\ &= \left[\frac{\partial S(V_0)}{\partial(q_1,q_2)}\right]V_1 + B(V_0)\dot{V}_1 + \left[\frac{\partial B(V_0)}{\partial(q_1,q_2)}\dot{V}_0\right]V_1 + P \end{aligned} \tag{12}$$

where $D_j=\partial D(\cdot,\cdot,\cdot)/\partial\{jth\ argument\}$; the symbol $[D_j]$ denotes the latter evaluated at $(V_0, \dot{V}_0, \ddot{V}_0)$ and square brackets [] are used to denote a matrix.

The first term $[\partial S/\partial(q_1,q_2)]V_1$ on the right-hand side of Eq. 12 is the stiffness term and corresponds to $K(t)$ in the text. The term $B(V_0)\dot{V}_1$ is the viscous term which corresponds to $B(t)$ in the text, and the term $[\partial B(V_0)/\partial(q_1, q_2)\dot{V}_0]V_1$ is referred to as the viscoelastic term. Since B is a matrix, the expression $\partial B(V_0)/\partial(q_1,q_2)$ is a 3-index tensor. Note that the viscoelastic term is largest in midreach where V_0 is large, and vanishes when $V_0=0$. If $B=const$, the viscoelastic term vanishes entirely. However, the presence of a viscoelastic term in the perturbation expansion shows that whenever the viscous force term of Eq. 8 is not constant this produces a non-negligible transient stiffness which must be inserted to represent the outcome of dynamic perturbations. While this term was not necessary to explain our data on reaching, it represents a potentially important theoretical prediction in situations which require adaptation to a viscous field.

Equation 12 is the variational equation mentioned in "Materials and methods." This equation gives the time varying linear relationship between the experimental perturbation $P(t)$ and the resulting change in the trajectory and its time derivatives. Despite the fact the original equation (Eq. 8) contained no explicit time dependence, and no new physical or physiological assumptions were used in deriving Eq. 12, each term in this equation depends on time through V_0.

Several forms were entertained for $S(q)$ in Eq. 8 including $S(q_1,q_2)=(Q_1(q_1),Q_2(q_2)$ for general cubic polynomials $Q_i(q)$, $i=1$, 2 and $S(q_1,q_2)=Kq$ for a constant matrix K. We also considered models of the form $S(q)=\nabla\sigma(q)$ where each of σ and ρ had the form

$$G(q_1,q_2) = aq_1^3 + bq_1^2q_2 + cq_1q_2^2 + dq_2^3 + eq_1^2 + fq_1q_2 + gq_2^2 + hq_1 + iq_2, \quad (13)$$

where $a, b, c, d, e, f, g, h, i$ are constants, different for each of σ and ρ. From the form $G(q_1,q_2)$, each of the terms on the right-hand side of Eq. 12 can be computed in a straightforward way. When $a=b=c=d=0$, in the scalar function $\sigma(q)$ the matrix $[\partial S(V_0)/\partial(q_1,q_2)]$ is constant and symmetric and when $a=b=c=d=0$ in the function $\rho(q)$, $B(V_0)$ is a constant symmetric matrix, and the viscoelastic term is zero.

Appendix B: torque estimation

This appendix describes the method used to estimate α, the total torque exerted by the human arm. If the inertial parameters of the human arm are known, net torque at each joint may be inferred directly from the kinematic variables by an algebraic substitution into the equation of motion (Spong and Vidyasagar 1989). However, net torque τ consists of the difference between the force exerted by the robot r (represented as human arm torque) and the torque exerted by the musculoskeletal components of the arm α; that is $\tau=\alpha-r$. The endpoint force d observed on the force sensor (with appropriate sign) is the active and inertial force exerted by the robot on the arm so that $r=J_q^t d$, where J_q is the jacobian of the transformation from (q_1,q_2) to (x,y) coordinates. Substituting for r gives $\alpha=\tau+J^t d$.

The arm/manipulandum system may be described by the equation:

$$D_r(s_1,s_2,\dot{s}_1,\dot{s}_2,\ddot{s}_1,\ddot{s}_2) = \rho + J_s^t(s_1,s_2)d$$
$$t = D_a(q_1,q_2,\dot{q}_1,\dot{q}_2,\ddot{q}_1,\ddot{q}_2) = \alpha - J_q^t(q_1,q_2)d \quad (14)$$

where s_1 and s_2 are robot joint angles, D_r and ρ are respectively the passive dynamics and driving torques exerted by the robot, D_a are the dynamical equations of the arm and the subscripts of J_s and J_q refer to the respective coordinate transformations for the robot and human arms. Thus, observations of d and a model of arm dynamics D_a are sufficient to estimate α for any ρ.

References

Bennet DJ (1993) Torques generated at the human elbow joint in response to constant position errors imposed during voluntary movements. Exp Brain Res 95:488–498

Bennet DJ (1994) Stretch responses in the human elbow joint during a voluntary movement. J Physiol (Lond) 474:339–351

Bennet DJ, Hollerbach JM, Xu Y, Hunter IW (1992) Time varying stiffness of human elbow joint during cyclic voluntary movement. Exp Brain Res 88:433–442

Bizzi E, Accornero N, Chapple W, Hogan N (1984) Posture control and trajectory formation during arm movement. J Neurosci 4:2738–2744

Colgate E, Hogan N (1989) An analysis of contact instability in terms of passive physical equivalents. In: IEEE Proc Int Conf Robotics and Automation, pp 404–409

Courant R, Hilbert D (1953) Methods of mathematical physics, vol I. Wiley, New York

Courant R, Hilbert D (1954) Methods of mathematical physics, vol II. Wiley, New York

Davison AC, Hinkley DV (1997) Bootstrap methods and their application. Cambridge, New York

Feldman AG (1966) Functional tuning of the nervous system during control of movement or maintenance of a steady posture. III. Mechanographic analysis of the execution by man of the simplest motor tasks, Biophysics 11:766–775

Flash T (1987) The control of hand equilibrium trajectories in multijoint movement. Biol Cybern 57:257–274

Forsythe GE (1977) Computer methods for mathematical computations. Prentice-Hall, Englewood Cliffs, NJ

Gomi H, Kawato M (1996) Equilibrium-point control hypothesis examined by measured arm stiffness during multijoint movement. Science 272:117–120

Gomi H, Kawato M (1997) Human arm stiffness and equilibrium-point trajectory during multi-joint movement. Biol Cybern 76: 163–171

Gomi H, Osu R (1998) Task-dependent viscoelasticity of human multijoint arm and its spatial characteristics for interaction with environments. J Neurosci 18:8965–8978

Gomi H, Koike Y, Kawato M (1992) Human hand stiffness during discrete point-to-point multijoint movements. Int Conf IEEE Eng Med Biol Soc

Gribble PL, Ostry DJ, Sanguinetti V, Laboissiere R (1998) Are complex control signals required for human arm movement? J Neurophysiol 79:1409–1424

Hodgson AJ, Hogan N (1999) Model-independent definition of attractor behavior applicable to interactive tasks. IEEE Trans Syst Man Cybern, part C: Appl and Rev (in press)

Hogan N (1985) The mechanics of multi-joint posture and movement control. Biol Cybern 52:315–331
Houk JC, Rymer WZ (1981) Neural control of muscle length and tension. In: Brooks VB (ed) Handbook of physiology, sect 1: the nervous system, vol II. American Physiological Society, Bethesda, MD
Johnson RA, Wichern DW (1988) Applied multivariate statistical analysis. Prentice-Hall, Englewood Cliffs, NJ
Karniel A, Inbar GF (1997) A model for learning human reaching movements. Biol Cybern 77:173–183
Katayama M, Kawato M (1993) Virtual trajectory and stiffness ellipse during multijoint arm movement predicted by neural inverse methods. Biol Cybern 69:353–362
Kawato M, Gomi H (1993) Feedback error learning model of cerebellar motor control. In: Mano N, Hamada I, Delong MR (eds) International symposium on the role of the cerebellum and basal ganglia in voluntary movement. Elsevier, New York
Kuo AD (1994) A mechanical analysis of force distribution between redundant, multiple degree of freedom actuators in the human: implications for the central nervous system. Hum Mov Sci 13:635–663
Lacquaniti F, Borghese NA, Carrozzo M (1992) Internal models of limb geometry in the control of hand compliance. J Neurosci 12:1750–1762
Latash ML (1994) Reconstruction of equilibrium trajectories and joint stiffness patterns during single-joint voluntary movements under different instructions. Biol Cybern 71:441–450
Lee CSG, Chung MJ (1984) An adaptive control strategy for mechanical manipulators. IEEE Trans Aut Cont AC 29:837–840
Lohmiller W, Slotine J-JL (1997) On contraction analysis for nonlinear systems. MIT-NSL Rep 962001
McConville JT, Churchill TD, Kaleps I, Clauser CE, Cuzzi J (1980) Anthropometric relationships of body and body segment moments of inertia. U.S. Department of Commerce National Technical Information Service. Springfield, Virginia
Milner TE (1993) Dependence of elbow viscoelastic behavior on speed and loading in voluntary movements. Exp Brain Res 93:177–180
Mussa-Ivaldi FA (1997) Nonlinear force fields: a distributed system of control primitives for representing and learning movements. Proc IEEE Int Symp Computational Intelligence in Robotics and Automation. Monterey, CA, pp 84–90
Mussa-Ivaldi FA, Giszter SF (1992) Vector field approximation: a computational paradigm for motor control and learning. Biol Cybern 67:491–500
Mussa-Ivaldi FA, Hogan N, Bizzi E (1985) Neural, mechanical and geometrical factors subserving arm posture in humans. J Neurosci 5:2732–2743
Mussa-Ivaldi FA, Giszter SF, Bizzi E (1994) Linear combinations of primitives in vertebrate motor control. Proc Natl Acad Sci U S A 91:7534–7538
Shadmehr R, Mussa-Ivaldi FA (1994) Adaptive representation of dynamics during learning of a motor task. J Neurosci 14: 3208–3224
Shadmehr R, Mussa-Ivaldi FA, Bizzi E (1993) Postural force fields of the human arm and their role in generating multi-joint movements. J Neurosci 13:45–62
Slotine JJE, Li W (1991) Applied nonlinear control. Prentice Hall, Englewood Cliffs, NJ
Spong MW, Vidyasagar M (1989) Robot dynamics and control. John Wiley and Sons, New York
Towhidkhah F, Gander RE, Wood HC (1997) Model predictive impedance control: a model for joint movement. J Motor Behav 29:209–222
Tsuji T, Morasso PG, Goto K, Ito K (1995) Human hand impedance characteristics during maintained posture. Biol Cybern 72: 475–485
Won J, Hogan N (1995) Stability properties of human reaching movements. Exp Brain Res 107:125–136